ELSEVIER

Effect of ion implantation on quantum well infrared photodetectors

N. Hatefi-Kargan [a],*, D.P. Steenson [a], P. Harrison [a], E.H. Linfield [a],
S. Khanna [a], S. Chakraborty [a], P. Dean [a], P.C. Upadhya [a], I. Farrer [b],
D.A. Ritchie [b], B. Sherliker [c], M. Halsall [c]

[a] *School of Electronic and Electrical Engineering, University of Leeds, Leeds LS2 9JT, UK*
[b] *Semiconductor Physics Group, Cavendish Laboratory, Madingley Road, Cambridge CB3 0HE, UK*
[c] *School of Electronic and Electrical Engineering, Sackville Street Building, University of Manchester, Manchester M60 1QD, UK*

Available online 17 November 2006

Abstract

Ion implantation is a postgrowth processing technique which, when combined with annealing, can be used to tune the absorption wavelength of quantum well devices. We have implanted and annealed, three different quantum well infrared photodetector structures, and measured the absorption spectra of the samples by Fourier transform spectroscopy. The peak absorption wavelength shift of each structure has been calculated as a function of diffusion length by simulating the diffusion processes. We found different diffusion rates for the structures and attribute this to different numbers of as-grown defects. Our results indicate that agglomeration of single defects into defect clusters limits the ability of ion implantation to tune the wavelength of a structure with a higher number of as-grown defects. Thus, a structure with the lowest number of as-grown defects is most useful for fabricating a multi-color quantum well photodetector by ion implantation, because in this case ion implantation can enhance the diffusion rate considerably leading to large red-shift in peak absorption wavelength.
© 2006 Elsevier B.V. All rights reserved.

PACS: 85.35.Be; 61.72.Vv; 85.60.GZ

Keywords: Quantum well photodetector; Quantum well intermixing; Ion implantation

1. Introduction

Since the first demonstration of quantum well infrared photodetectors (QWIPs) in 1987 [1,2], there has been rapid development in this field. Indeed multi-color detection by QWIPs is now important for measuring temperature, chemical analysis, target discrimination and identification [3]. Multi-color detection by QWIPs can be achieved by growing stacks of quantum wells where each stack is sensitive to a particular band [4–6]. This technique requires complicated processing steps which increases the cost of these devices. As an alternative, quantum well intermixing techniques [7] are capable of tuning the absorption wave-length of quantum wells after growth. The techniques have been used successfully in fabricating optoelectronic devices [8–12] such as lasers and waveguides. Quantum well intermixing techniques include [7]: laser induced disordering, impurity free vacancy disordering, impurity induced disordering and ion implantation induced disordering, and each has been used to tune the detection wavelength of QWIPs [13–19]. Amongst the various intermixing techniques, ion implantation induced disordering is preferred because it is more controllable than the others.

We have modelled the effect of diffusion on the red-shift in the absorption wavelength of quantum well photodetectors by solving both the diffusion equation and Schrödinger's equation on a region containing one quantum well. We have also studied experimentally the effect of implantation on three different structures to see how the structure and growth conditions affect the degree of wavelength shift.

* Corresponding author. Tel.: +44 (0) 113 2440896; fax: +44 (0) 113 3432070.
E-mail address: eennhk@leeds.ac.uk (N. Hatefi-Kargan).

Results from this study are presented here. Implantation was undertaken with different doses of 1700 keV hydrogen molecules and followed by annealing in a rapid thermal annealer (RTA) at 950 °C, which is the optimum temperature for intermixing GaAs/AlGaAs quantum well structures [13]. Hydrogen molecules were used because light atoms create more point defects during implantation rather than defect clusters [20]. Point defects enhances diffusion, as is needed for intermixing quantum wells, whilst defect clusters do not. Simulation by SRIM software [21], which is software based on a Monte Carlo method for calculating the distribution of implanted ions and the damage created inside a material, indicate that at a 1700 keV implantation energy almost all of the implanted ions pass through the structures and gather inside the substrate and also the defects produced inside the active region of our QWIPs are approximately uniform. This is important in order to not to broaden the absorption line shape of the structures. In our research, Fourier transform infrared spectroscopy (FTIR) was used to measure absorption spectra of the samples. By fitting the simulation results to the experimental values, diffusion coefficients were then calculated.

2. Modelling diffusion

In a GaAs/AlGaAs structure, Al diffuses from barriers to the wells and Ga diffuses from the wells to the barriers. This diffusion changes the well shape, resulting in a variation in the energy levels that an electron can occupy (Figs. 1 and 2). Therefore, the absorption wavelength of the structures changes.

Diffusion is described by the equation:

$$\partial C(z,t)/\partial t = \frac{\partial}{\partial z}(D\partial C(z,t)/\partial z) \tag{1}$$

where $C(z,t)$ is the concentration of the diffusing atom which is function of z and t. z is the distance in growth direction and t is the time duration of diffusion. In our work, $C(z,t)$ will be considered as the mole fraction of the Al inside the material, with D being the diffusion coefficient of the diffusing atom, which will be assumed to be
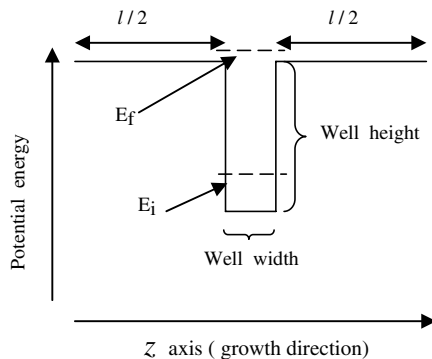

Fig. 1. The conduction band of a GaAs layer (well) sandwiched between two AlGaAs layers (barriers). E_i, and E_f are schematic initial and final energy levels of an electron in this structure.
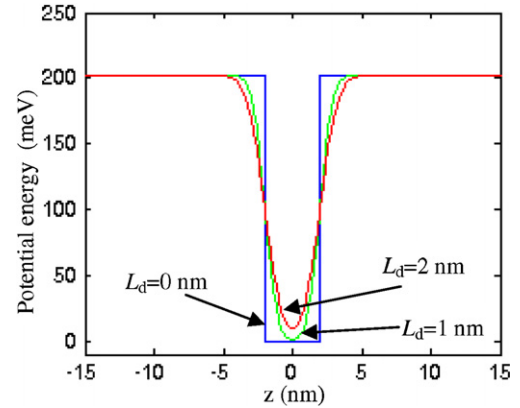

Fig. 2. The change in shape of the conduction band of a GaAs/AlGaAs quantum well during diffusion: before diffusion ($L_d = 0$ nm); and after diffusion for $L_d = 1$ nm, and $L_d = 2$ nm.

constant. The dependence in the *x*- and *y*-directions has been ignored by assuming that there is no gradient along these directions.

Energy levels that an electron can occupy can be calculated by solving the Schrödinger equation:

$$\frac{\partial}{\partial z}\left(\frac{\hbar}{2m^*}\partial\Psi(z)/\partial z\right) + V(z)\Psi(z) = E\Psi(z) \tag{2}$$

where $\Psi(z)$ is the wave function, and $V(z)$ is the potential energy of an electron in the *z*-direction and m^* is the effective mass of the electron, which is a function of z. For simulation, the region shown in Fig. 1 was considered, and Eqs. (1) and (2) solved by the finite difference method.

For the diffusion equation we write:

$$C(z_i, t + \delta t) = C(z_i, t)$$
$$+ 2D\delta t\left\{\frac{C(z_{i+1}, t) - C(z_i, t)}{h_{i+1}(h_i + h_{i+1})} + \frac{C(z_{i-1}, t) - C(z_i, t)}{h_i(h_i + h_{i+1})}\right\} \tag{3}$$

and for the Schrödinger equation:

$$\left\{\left[\frac{2\hbar^2}{h_k[m^*(z_{i-1}) + m^*(z_i)](h_i + h_{i+1})} + \frac{2\hbar^2}{h_{i+1}[m^*(z_i) + m^*(z_{i+1})](h_i + h_{i+1})}\right.\right.$$
$$\left.+ \frac{-2\hbar^2}{h_i[m^*(z_{i-1}) + m^*(z_i)](h_i + h_{i+1})}\right]\psi(z_{i-1})$$
$$+ \left\{\frac{2\hbar^2}{h_k[m^*(z_{i-1}) + m^*(z_i)](h_i + h_{i+1})}\right.$$
$$+ \frac{2\hbar^2}{h_{i+1}[m^*(z_i) + m^*(z_{i+1})](h_i + h_{i+1})} + V(z_i)\right\}\psi(z_i)$$
$$\left.+ \frac{-2\hbar^2}{h_{i+1}[m(z_i) + m(z_{i+1})](h_i + h_{i+1})}\psi(z_{i+1}) = E\psi(z_i)\right\} \tag{4}$$

where '*i*' is a common point in the simulation region and z_i is the coordinate of that point on the z-axis, $h_i = z_i - z_{i-1}$, and E is the energy level that an electron can occupy. The advantage of discretizing in this form is that divergence does not occur because of the discontinuity of electron effective mass at the boundaries between the wells and barriers [22]. The diffusion length, $L_d = 2\sqrt{Dt}$, [23] was used as

the parameter to describe the diffusion process. As boundary conditions it was assumed that the mole fraction of Al does not change during the diffusion at both end points of the region shown in Fig. 1, and it was also assumed that the wave functions are zero at these points. The parameter l in Fig. 1 is considered to be equal to barrier width for solving diffusion equation but for solving Schrödinger's equation it was considered large enough so that convergence happened. In our calculation, peak absorption wavelength is considered as a transition from the initial energy level to the final energy level where the oscillator strength [24,25] is maximum. The bottom of the potential well is narrowed during diffusion and moves up in energy (Fig. 2). This causes the initial energy level to increase (Fig. 3). In contrast widening of the top of the well causes the final energy level to move down in energy (Fig. 4). Two structures were studied in this work, one with 50 nm wells and the other with 40 nm wells. The first one was a 50 period multi-quantum well structure with 5 nm GaAs wells and 30 nm undoped $Al_{0.29}Ga_{0.71}As$ barriers. The central 3.5 nm of each well was Si doped at a level of 5.5×10^{17} cm^{-3}, and the structure was designed to have an absorption peak at 8 μm. The active layers were sandwiched between 1 and
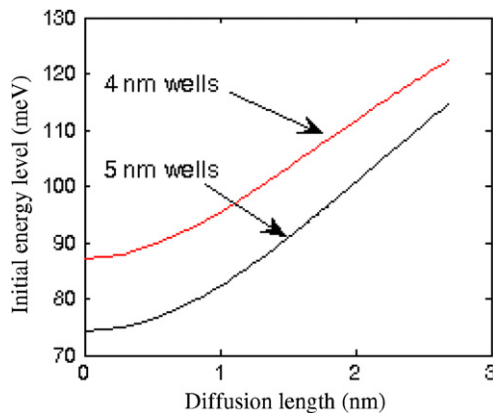
Fig. 5. Predicted red-shift of the peak absorption wavelength of the structures with 5 nm (wafer A and B) and 4 nm (wafer C) wells as a function of diffusion length. The 'staircase' structure in wafer C is an artifact of calculation.

1.5 μm GaAs layers Si doped at 1×10^{18} cm^{-3} in order to provide top and bottom contacts respectively. The second structure was a 50 period multi-quantum well structure with 4 nm GaAs wells and 50 nm undoped $Al_{0.27}Ga_{0.73}As$ barriers. The central 2.5 nm of each well in this case was doped at 1.2×10^{18} cm^{-3}, and the structure was designed to have an absorption peak at 9 μm. The same contacting layers were then used for the top and bottom of the active region. For the first structure, two wafers were grown: wafer A at 650 °C and wafer B at 600 °C. The wafer of the second structure, wafer C, was grown at 625 °C. For the structure with 5 nm wells the final energy level is matched to the top of the well and as diffusion occurs, there is a continuous decrease in the position of this energy level. In contrast, the structure with 4 nm wells is a bound to continuum QWIP and so the final energy level is above the top edge of the well. Now, as diffusion occurs, the position of this energy level falls in discrete steps, owning to the discreteness of energy levels above the quantum wells which is a result of applied boundary conditions in our modelling. The predicted variation of peak absorption wavelength with diffusion length is plotted for the both structures in Fig. 5.

3. Samples and experimental method

Samples from each wafer were implanted with 1700 keV hydrogen molecules at range of different doses. Tables 1–3 give further details. With this implantation energy, from SRIM simulations the density of implanted ions in the active region of the structure with 4 nm wells is below 0.06% of the density of the ions at the peak position (Fig. 6) and the densities of gallium and aluminium vacancies (Fig. 7) are approximately uniform. A similar conclusion is reached for the structure with 5 nm wells as well, because the active region of this structure is thinner.

Samples were caped between two silicon wafers and annealed by an RTA with the system programmed to ramp

Fig. 3. Position of initial energy level of the structures with 5 nm (wafer A and B) and 4 nm (wafer C) wells as a function of diffusion length.
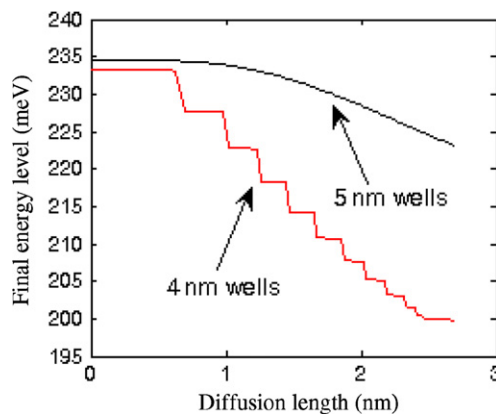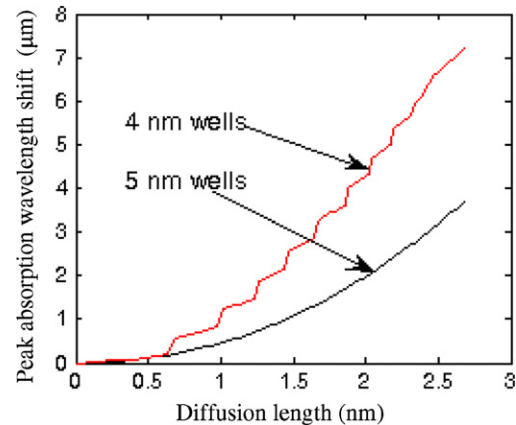
Fig. 4. Position of final energy level of the structures with 5 nm (wafer A and B) and 4 nm (wafer C) wells as a function of diffusion length. The 'staircase' structure in wafer C is an artifact of calculation.

Table 1
Samples from wafer A

Sample	Implantation dose (cm^{-2})	Annealing time	Peak absorption wavelength (μm)
A-1	Not implanted	Not annealed	7.9
A-2	Not implanted	15 s	8.1
A-3	Not implanted	30 s	8.4
A-4	Not implanted	45 s	8.7
A-5	3×10^{16}	30 s	–
A-6	5×10^{16}	30 s	–

Table 2
Samples from wafer B

Sample	Implantation dose (cm^{-2})	Annealing time	Peak absorption wavelength (μm)
B-1	Not implanted	Not annealed	7.8
B-2	Not implanted	15 s	8.7
B-3	Not implanted	30 s	9.5
B-4	Not implanted	60 s	10.8
B-5	1×10^{15}	30 s	9.7
B-6	5×10^{15}	30 s	9.8
B-7	1×10^{16}	30 s	9.4

Table 3
Samples from wafer C

Sample	Implantation dose (cm^{-2})	Annealing time	Peak absorption wavelength (μm)
C-1	Not implanted	Not annealed	9.0
C-2	Not implanted	15 s	9.6
C-3	Not implanted	30 s	10.5
C-4	Not implanted	60 s	11.1
C-5	1×10^{15}	30 s	10.8
C-6	5×10^{15}	30 s	11.3
C-7	1×10^{16}	30 s	11.3

Fig. 7. Distribution of aluminium gallium vacancies as a function of implantation depth for structures with 5 nm wells (wafers A and B). The high lighted window on the figure includes the active region of the structure.

up to 950 °C in 30 s, remain at 950 °C for different annealing times, as indicated in Tables 1–3 and then ramp down to room temperature in 30 s. Ramping up to 950 °C in 30 s and ramping down to room temperature in 30 s was shown not to cause any cracking in the GaAs. For each sample both ends of the 5×9 mm chips were polished at 45°, in order for samples to act as a waveguide. Infrared light was then coupled into and transmitted through the samples, and the spectra of the samples obtained at room temperature by Fourier transform spectroscopy [2].

4. Results

Fig. 8 shows the absorption spectra of an as-grown sample from wafer A (spectra A1). Two absorption peaks are observed, one at approximately 8 μm and the other at 10.8 μm. Photocurrent spectra from the sample (Fig. 9) show only one peak, and this can be attributed to the expected intersubband transition which is at approximately 8 μm. The second absorption peak in Fig. 8 is therefore a
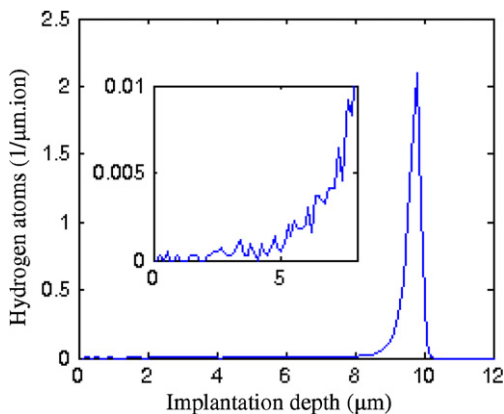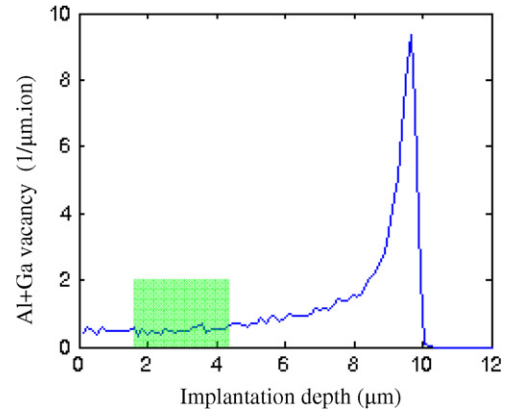

Fig. 6. Simulated distribution of implanted hydrogen atoms as a function of implantation depth for structure with 4 nm wells (wafer C). Inset: simulated data for depths between 0 and 7 μm on an enlarged scale.
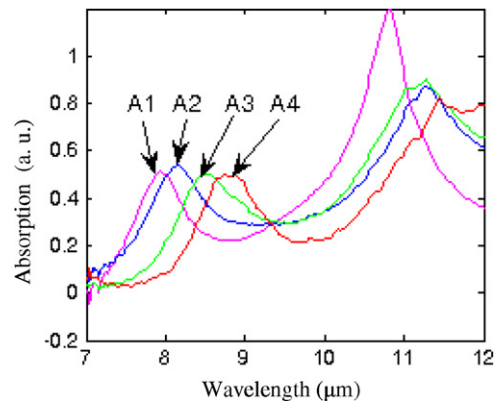

Fig. 8. Room temperature absorption spectra of unimplanted samples (see Table 1) from wafer A: A1 (unannealed), A2 (15 s anneal), A3 (30 s anneal), and A4 (45 s anneal).
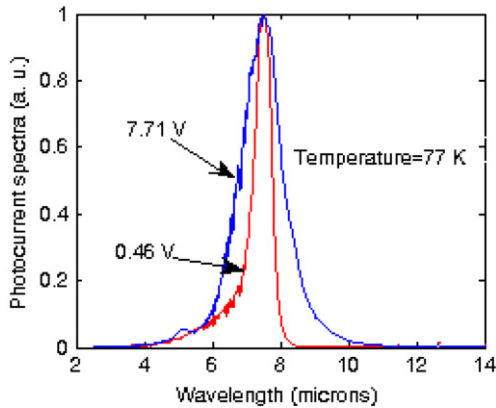
Fig. 9. Photocurrent spectra of an as-grown sample from wafer A at 77 K for two different bias voltages: 0.46, and 7.71 V.

Fig. 11. Calculated diffusion coefficients of the samples from wafer B and wafer C implanted with different doses and annealed at 950 °C for 30 s.

result of another mechanism which is not related to inter-subband transitions. Since if it originated from inter-subband transition then the peak would be expected to appear on the photocurrent spectra as well. Further investigation is needed to confirm the origin of the 10.8 μm peak, but it is likely to be a result of plasmon excitation.

Fig. 8 shows the effect of annealing on unimplanted samples from wafer A, with equivalent data being presented for wafer B in Fig. 10a. Despite wafer A and wafer B incorporating identical active regions, the unimplanted intermixing in wafer A, is clearly lower than in wafer B. The enhanced diffusion in the later is likely to caused by the as-grown defects in this structure being higher [26].

It has been pointed out [27] that, at lower implantation doses single vacancy and defect densities increase with implantation dose, and so the diffusion rate increases with increasing implantation dose. However beyond a critical value, increasing the implantation dose decreases the single vacancy and defect density by forming defect clusters, and the diffusion rate then decreases with increased implantation dose. If there is a higher amount of as-grown defects
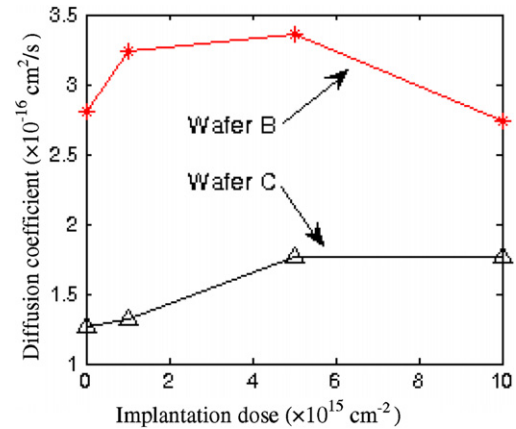
in wafer B, then the additional defects created by implantation, for doses up to 5×10^{15} cm^{-2}, will only add a small additional density of single vacancies and defects, and hence the diffusion rate is only enhanced slightly (Fig. 10b). In this case for an implantation dose of 5×10^{15} cm^{-2}, diffusion coefficient is increased by a factor of 1.19 compared to the unimplanted value (Fig. 11). Then if the implantation dose is increased beyond a critical value (in this case beyond 5×10^{15} cm^{-2}), the diffusion rate is decreased which can be related to the agglomeration of single defects to defect clusters.

Enhancement of diffusion in wafer C is considerable, as shown in Fig. 12, relative to structure B, and the diffusion coefficient is increased by a factor of 1.4, compared to the unimplanted value, for an implantation dose of 5×10^{15} cm^{-2}. The critical implantation dose for wafer C (1×10^{16} cm^{-2}), is also higher than the critical implantation dose for wafer B (5×10^{15} cm^{-2}), indicating that the number of as-grown defects inside wafer C is lower than the number of as-grown defects inside the wafer B. We could not measure room temperature absorption spectra of the
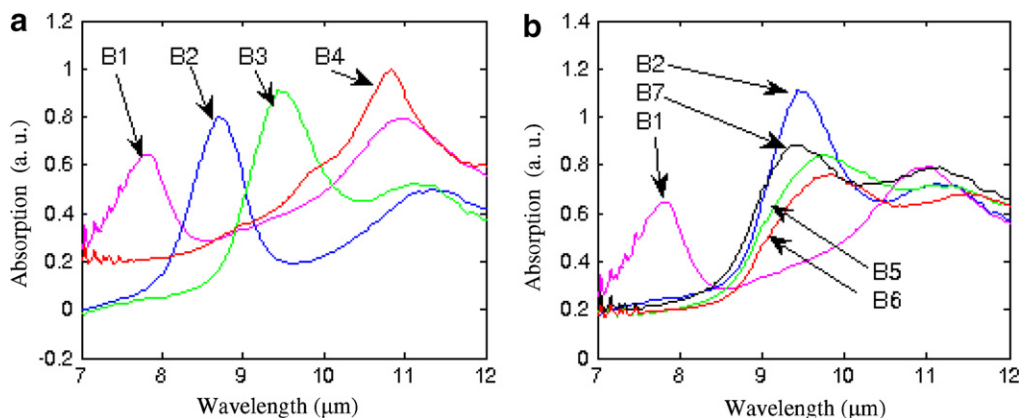

Fig. 10. Room temperature absorption spectra of samples (see Table 2) from wafer B. (a) Unimplanted data: B1 (unannealed), B2 (15 s anneal), B3 (30 s anneal), and B4 (60 s anneal); and (b) comparison of implanted and unimplanted data: B1 (unimplanted, unannealed), B3 (unimplanted, 30 s anneal), B5 (implanted 1×10^{15} cm^{-2}, 30 s anneal), B6 (implanted 5×10^{15} cm^{-2}, 30 s anneal), and B7 (implanted 1×10^{16} cm^{-2}, 30 s anneal).
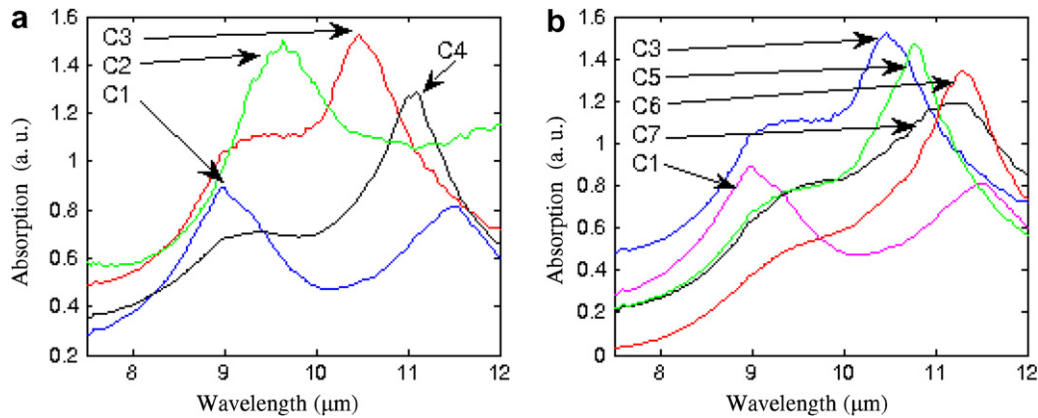
Fig. 12. Room temperature absorption spectra of samples (see Table 3) from wafer C. (a) Unimplanted data: C1 (unannealed), C2 (15 s anneal), C3 (30 s anneal), and C4 (60 s anneal); and (b) comparison of implanted and unimplanted data: C1 (unimplanted, unannealed), C3 (unimplanted, 30 s anneal), C5 (implanted 1×10^{15} cm^{-2}, 30 s anneal), C6 (implanted 5×10^{15} cm^{-2}, 30 s anneal), and C7 (implanted 1×10^{16} cm^{-2}, 30 s anneal).

samples from wafer A implanted with doses at 3×10^{16} and 5×10^{16} cm^{-2}. There might be two reasons for the disappearance of the absorption peaks. First the quantum wells might be intermixed highly during annealing, so that the absorption peak is at longer wavelengths and is not measurable at room temperature owing to phonon scattering, or the structure is completely intermixed during annealing and there is no quantum well structure to give an absorption peak. Alternatively, the level of defects created by implantation might be so high that the absorption peak is very low owing to the scattering of electrons by defects, and hence not measurable. If it is assumed that the diffusion coefficient is proportional to the vacancy density, then the diffusion coefficient of the sample implanted with a dose of 3×10^{16} cm^{-2} will be at most 5.3×10^{-16} cm^2/s. Inserting this diffusion coefficient into the diffusion equation and simulating the diffusion process shows that after diffusion for a 30 s diffusion period, the quantum wells are not completely intermixed and the absorption peak is at 11.2 μm. This absorption peak is measurable at room temperature. Therefore it is likely that scattering by defects explains the disappearing of the absorption peak.

5. Conclusion

We have modelled the effect of diffusion on the absorption QWIPs and have investigated experimentally the effect of intermixing on different QWIP structures grown under different growth conditions. Our results indicate that greater intermixing occurs in unimplanted structures with higher as-grown defects, and ion implantation then only enhances the diffusion rate slightly. Indeed enhancement only takes place if the implantation dose is sufficiently low, otherwise the diffusion rate decreases. Thus in order to fabricate multi-color quantum well photodetectors by ion implantation, there is a critical need for the structures to be grown under optimum growth condition with the lowest possible number of as-grown defects. Ion implanta-

tion can then enhance the diffusion considerably, which is a requirement for fabricating multi-color photodetectors.

References

[1] B.F. Levine, K.K. Choi, C.G. Bethea, J. Walker, R.J. Malik, Appl. Phys. Lett. 50 (1987) 1092.
[2] B.F. Levine, R.J. Malik, J. Walker, K.K. Choi, C.G. Bethea, D.A. Kleinman, J.M. Vanderberg, Appl. Phys. Lett. 50 (1987) 273.
[3] X.D. Jiang, S.S. Li, M.Z. Tidrow, IEEE J. Quantum Electron. 35 (1999) 1685.
[4] S.V. Bandara, S.D. Gunapala, J.K. Liu, S.B. Rafol, D.Z. Ting, J.M. Mumolo, R.W. Chuang, T.Q. Trinh, J.H. Liu, K.K. Choi, M. Jhabvala, J.M. Fastenau, W.K. Liu, Infrared Phys. Technol. 44 (2003) 369–375.
[5] P. Bois, E. Costard, X. Marcadet, E. Herniou, Development of quantum well infrared photodetectors in France, Infrared Phys. Technol. 42 (2001) 291.
[6] J. Jiang, S.S. Li, M.Z. Tidrow, W.R. Dyer, W.K. Liu, J.M. Fastenau, T.R. Yurasits, Appl. Phys. Lett. 79 (2001) 2982.
[7] J.H. Marsh, Semicond. Sci. Tech. 8 (1993) 1136.
[8] S. Charbonneau, E.S. Koteles, P.J. Poole, J.J. He, E.C. Aers, J. Haysom, M. Buchanan, Y. Feng, A. Delage, F. Yang, M. Davies, R.D. Goldberg, P.G. Piva, I.V. Mitchell, IEEE J. Sel. Top. Quant. 4 (1998) 772.
[9] O. Gunawan, T.K. Ong, Y.W. Chen, B.S. Ooi, Y.L. Lam, Y. Zhou, Y.C. Chan, Surf. Coat. Tech. 130 (2000) 116.
[10] D. Hofstetter, B. Maisenholder, H.P. Zappe, IEEE J. Sel. Top. Quant. 4 (1998) 794.
[11] B.S. Ooi, S.G. Ayling, A.C. Bryce, J.H. Marsh, IEEE Photon. Tech. L. 7 (1995) 944.
[12] M. Paquette, V. Aimez, J. Beauvais, J. Beerens, P.J. Poole, S. Charbonneau, A.P. Roth, IEEE J. Sel. Top. Quant. 4 (1998) 741.
[13] L. Fu, H.H. Tan, C. Jagadish, N. Li, N. Li, X. Liu, W. Lu, S.C. Shen, Infrared Phys. Technol. 42 (2001) 171.
[14] M.B. Johnston, M. Gal, N. Li, Z.H. Chen, X.Q. Liu, N. Li, W. Lu, S.C. Shen, L. Fu, H.H. Tan, C. Jagadish, Appl. Phys. Lett. 75 (1999) 923.

[15] N. Li, N. Li, W. Lu, X.Q. Liu, X.Z. Yuan, Z.F. Li, H.F. Dou, S.C. Shen, Y. Fu, M. Willander, L. Fu, H.H. Tan, C. Jagadish, M.B. Johnston, M. Gal, Superlattice. Microst. 26 (1999) 317.

[16] X.Q. Liu, N. Li, W. Lu, N. Li, X.Z. Yuan, S.C. Shen, L. Fu, H.H. Tan, C. Jagadish, Jpn. J. Appl. Phys. 1 39 (2000) 1687.

[17] D. Sengupta, V. Jandhyala, S. Kim, W. Fang, J. Malin, P. Apostolakis, K.C. Hseih, Y.C. Chang, S.L. Chuang, S. Bandara, S. Gunapala, M. Feng, E. Michielssen, G. Stillman, IEEE J. Sel. Top. Quant. 4 (1998) 746.

[18] D.K. Sengupta, T. Horton, W. Fang, A. Curtis, J. Li, S.L. Chuang, H. Chen, M. Feng, G.E. Stillman, A. Kar, J. Mazumder, L. Li, H.C. Liu, Appl. Phys. Lett. 70 (1997) 3573.

[19] A.G. Steele, M. Buchanan, H.C. Liu, Z.R. Wasilewski, J. Appl. Phys. 75 (1994) 8234.

[20] H.H. Tan, J.S. Williams, C. Jagadish, P.T. Burke, M. Gal, Appl. Phys. Lett. 68 (1996) 2401.

[21] http://www.srim.org/.

[22] P. Harrison, Quantum Wells, Wires and Dots, Prentice Hall, 1999.

[23] M.E. Glicksman, Diffusion in Solids: Field Theory, Solid-state Principles, and Applications, Wiley, 2000.

[24] K.K. Choi, J. Appl. Phys. 73 (1993) 5230.

[25] K.K. Choi, The Physics of Quantum Well Infrared Photodetectors, World Scientific, 1997.

[26] J.E. Haysom, G.C. Aers, S. Raymond, P.J. Poole, J. Appl. Phys. 88 (2000) 3090.

[27] P.J. Poole, P.G. Piva, M. Buchanan, G.C. Aers, A.P. Roth, M. Dion, Z.R. Wasilewski, E.S. Koteles, S. Charbonneau, J. Beauvais, Semicond. Sci. Tech. 9 (1994) 2134.